UC Irvine
UC Irvine Previously Published Works

Title

Association Between the Size and 3D CT-Based Radiomic Features of Breast Cancer Hepatic Metastasis

Permalink

https://escholarship.org/uc/item/7ht4321f

Journal

Academic Radiology, 28(4)

ISSN

1076-6332

Authors

Velichko, Yuri S
Mozafarykhamseh, Amirhossein
Trabzonlu, Tugce Agirlar
et al.

Publication Date

2021-04-01

DOI

10.1016/j.acra.2020.03.004

Peer reviewed

Association Between the Size and 3D CT-Based Radiomic Features of Breast Cancer Hepatic Metastasis

Yuri S. Velichko, PhD[1,2], **Amirhossein Mozafarykhamseh, MD**[2], **Tugce Agirlar Trabzonlu, MD**[1], **Zhuoli Zhang, MD, PhD**[1,2], **Alfred W. Rademaker, PhD**[3], **Vahid Yaghmai, MD**[1,2]

[1]Department of Radiology, Northwestern University Feinberg School of Medicine, Chicago, Illinois

[2]Quantitative Imaging Core Lab, Department of Radiology, Northwestern University Feinberg School of Medicine, Chicago, Illinois

[3]Department of Preventive Medicine, Northwestern University Feinberg School of Medicine, Chicago, Illinois

Abstract

Purpose: To evaluate the effect of the anatomic size on 3D radiomic imaging features of the breast cancer hepatic metastases.

Materials and Methods: CT scans of 81 liver metastases from 54 patients with breast cancer were evaluated. Ten most common 3D radiomic features from the histogram and gray level co-occurrence matrix (GLCM) categories were calculated for the hepatic metastases (HM) and compared to normal liver (NL). The effect of size was evaluated by using linear mixed-effects regression models. The effect of size on different radiomic features was analyzed for both liver lesions and background liver.

Results: Three-dimensional radiomic features from GLCM demonstrate an important size dependence. The texture-feature size dependence was found to be different among feature categories and between the HM and NL, thus demonstrating a discriminatory power for the tissue type. Significant difference in the slope was found for GLCM homogeneity (NL slope = 0.004, slope difference 95% confidence interval [CI] 0.06-0.1, $p<0.001$), contrast (NL slope = 45, slope difference 95% CI 205-305, $p<0.001$), correlation (NL slope = 0.04, slope difference 95% CI 0.11-0.21, $p<0.001$), and dissimilarity (NL slope = 0.7, slope difference 95% CI 3.6-5.4, $p<0.001$). The GLCM energy (NL slope = 0.002, slope difference 95% CI −0.0005 to −0.0003, $p<0.007$), and entropy (NL slope = 1.49, slope difference 95% CI 0.07-0.52, $p<0.009$) exhibited size-dependence for both NL and HM, although demonstrating a difference in the slope between themselves.

Conclusion: Radiomic features of breast cancer hepatic metastasis exhibited significant correlation with tumor size. This finding demonstrates the complex behavior of imaging features and the need to include feature-specific properties into radiomic models.

Correspondence: Yuri S. Velichko, PhD, Department of Radiology, Northwestern University Feinberg School of Medicine, Chicago, Illinois, y-velichko@northwestern.edu.

Keywords

Computed tomography; Features; Gray levels; Radiomics; Texture; Tumor size

Introduction

Quantitative oncologic imaging continues to gain immense importance in clinical radiology. Today, a number of imaging measurements such as a size, density, metabolic activity, diffusion, or permeability parameters are commonly used as surrogate endpoints for tumor characterization and assessment of response to therapy (1, 2, 3, 4). They provide noninvasive assessment of clinical results with reasonable accuracy and reproducibility. The current practice to assess response to therapy in solid tumors is based on the monitoring of the tumor size according to Response Evaluation Criteria in Solid Tumors (RECIST). Today, RECIST is the most commonly used anatomic imaging biomarker in oncologic clinical trials (2,3). However, it has been demonstrated that the response to therapy based on size measurements may not reflect true response to therapy in cancers such as lymphomas, sarcoma, gastrointestinal stromal tumor (5), and for some therapies may show discordance with pathologic response (6). Also, the use of tumor size alone has certain limitations as shown in various studies (7, 8, 9).

Radiomics is a rapidly developing and expanding field in oncologic imaging (10). It aims to maximize the prognostic utility of measurable and quantifiable imaging properties, also known as radiomic features. These features are first, second, or higher-order statistical outputs of various image-processing and data-characterization algorithms. Radiomic features are designed to capture the unique characteristics of diseased or malignant tissue through the quantification of various image-texture properties like randomness, coarseness, directionality, to name a few (11,12). It is currently assumed that tumor heterogeneities are associated with the underlying tumor genotype and phenotype (13,14). Therefore, quantification of the tumor texture can provide a more detailed and distinctive description of tumor image properties in comparison to anatomic imaging biomarkers (15). In particular, the first-order features are computed using the distribution of voxel intensities in a region or a volume of interest (ROI or VOI), while the second-order features (e.g., GLCM) quantify the spatial arrangement of the voxel-intensity levels in the texture image. Numerous studies have utilized radiomic approach for various types of cancers by using different imaging modalities. It has been demonstrated that some radiomic features or a combination of features are associated with clinically relevant information. For example, several studies have shown that the first-order features can differentiate between the cancer subtypes or the grades of malignancy (16). Second-order features have shown correlations with the response to therapy (17,18), malignancy classification (19), molecular subtypes (20), and genomic data (21). For that reason, radiomics holds a great promise toward the development of comprehensive imaging biomarkers (22,23).

Many radiomic features are sensitive to scanning techniques, reconstruction algorithms, image spatial resolution, as well as segmentation methodology. A number of studies investigated the sensitivity of radiomic features on the scan reconstruction parameters by

varying the voxel size and slice thickness. They proposed various feature-normalization techniques to reduce this dependence (24–27). Also, in a similar manner, some recent studies demonstrated the dependence of radiomic features on the number of voxels inside the VOI (27). Proposed correction algorithms helped to reduce the VOI volume dependence and improve the inter-reader variability. While these studies have focused on addressing the image reconstruction-related questions, the VOI volume dependence of radiomic features might be also related to changes in the tumor tissue associated with the tumor growth and the development of heterogeneities in response to the therapy, for example. Therefore, the main objective of our study is to examine the interaction between computed tomography [CT]-derived 3D texture features and anatomic tumor volume as a measure of tumor size. In order to minimize the interscan or image reconstruction variability, the images were obtained on the same CT scanner using the same imaging protocol.

Materials and Methods

Study Population

Northwestern University Institutional Review Board (IRB) approved this retrospective study and waived the requirement for informed consent. Patients with diagnosed breast cancer were identified from the enterprise data warehouse after IRB approval. The cohort used in this study consisted of 54 patients with breast cancer of three primary molecular subtypes (luminal, HER2-positive, and triple-negative). To exclude interscan variability associated with the differences in imaging equipment or the imaging protocol, contrast-enhanced CT scans were obtained retrospectively from patients with imaging performed using the same scanner and imaging protocol. Patients underwent a wide range of treatments for different time periods at the moment of imaging. Adjuvant treatment included Tamoxifen (25%), Trastuzumab (20%), Anastrozole (16%), Paclitaxel (14%), Palbociclib (11%), Palbociclib/Letrozole (6%), Capecitabine (4%), and Docetaxel/ Bevacizumab (4%), where the percentage gives the total proportion of subjects in each treatment group. The average age of the patients was 57 ± 11 years ranging from 39 to 87 years.

Imaging Technique

Contrast-enhanced CT scans were obtained with multidetector CT scanners(Siemens SOMATOM Force, 192-slice) using the same imaging protocol. CT examinations were performed at a fixed tube potential of 100 kV and a reference current of 250 mA. In all instances, the slice thickness for the reconstructed images was 5 mm, the average voxel (pixel) size was 0.64 mm ranging from 0.5 mm to 0.85 mm and the spiral pitch was 0.6. Axial contrast-enhanced CT scan were obtained in the venous phase (40 seconds after initiation of intravenous contrast injection). Nonionic contrast material (iohexol 350, Omnipaque; GE Healthcare or iopamidol 370, Isovue; Bracco, Plainsboro, NJ) was injected intravenously at a rate of 3 mL/second for a total of 125 mL. Images were retrieved from the imaging archive (PACS, GE Centricity, General Electric, Milwaukee, WI).

Image Segmentation and Feature Extraction

The volumetric segmentation and 3D texture analyses was performed for each tumor using LIFEx software, version 3.74 (http://www.lifexsoft.org; Orsay, France) (28). A maximum of

two well-defined and well-separated metastases with the longest diameter greater than 5 mm were selected with total of 81 metastases in 54 patients. Up to two lesions per patient were selected. VOI was manually drawn by one experienced radiologists (5 years of experience in volumetric CT segmentation) along the margin of the lesion (Figure 1) on each consequent slice containing the tumor. Once the tumor texture was assessed the VOI was moved to the normal liver avoiding vascular structures and other lesions. The texture of the normal liver was used as a reference. In 12 cases, it was difficult to accommodate the whole VOI within the normal liver and a new VOI of a similar size and shape was created using an original VOI. First, the original VOI was moved to a region of the liver with the minimal presence of vascular structures or other lesions. Next, the overlapping margins of the VOI were cropped to remove the vascular or other tumor tissue, while new volumes from the normal liver were added to equate the "new" VOI to the "old" one in terms of the size. Prior to texture analysis, spatial resampling was performed to obtain in-plane spacing of 0.64 mm (the average in-plane voxel size) in both directions. CT intensities within the VOI were normalized between $\mu-3\sigma$ and $\mu+3\sigma$ and reduced to 128 gray-levels (7-bits), where μ is the mean value inside the VOI and σ is the standard deviation.

The radiomic features included first-order histogram based features (mean attenuation, standard deviation (SD), gray-level histogram skewness, and kurtosis) and second-order 3D gray-level co-occurrence matrix (GLCM) features (homogeneity, energy, contrast, correlation, entropy, and dissimilarity) (28). First introduced by Haralick in 1973 (29), these features are the most commonly used and have proven to be effective texture discriminators (30). The 3D GLCM was calculated using separation offset equal to 1 voxel and 13 different directions. All elements of GLCM were normalized so that the sum of its elements was equal to 1. In order to gain orientation invariance, the GLCM features were averaged over all directions.

Statistical Analysis

In our study, we did simultaneous measurements of hepatic metastasis and normal liver tissue and, therefore, the same patient measurements were considered as paired. A skewness (SE), kurtosis (RKU), Shapiro-Wilk's test (normality indicated if $p>0.05$), a visual inspection of normal Q-Q plots and box plots were conducted to test normality of measurements. The Spearman's rank-correlation test was conducted to assess the degree of correlation between the texture features and VOI's volume. The Levene's test was performed to test for equality of variance between hepatic metastases and normal liver. For normally distributed features with equal variances the t-test was used to compare features between hepatic metastases (HM) and normal liver (NL). Otherwise, we conducted Mann-Whitney U test, as a nonparametric alternative to the t-test.

To test the hypothesis that the radiomic features depend on the tumor size we used a linear mixed-effects (LME) regression analysis. To utilize a linear regression analysis, first, we examined the functional relationships between the texture features and the VOI volume by using five fitting models:– linear, logarithmic, inverse, power, and exponential. The coefficient of determination, R-squared, was computed to assess the goodness of each model. For each fitted model, the normality of the residuals was tested with the Shapiro-

Wilk's test and a visual inspection of normal Q-Q plots. The best fitting-model for each feature was selected based on the highest R-squared and passing the normality test of residuals.

For each feature, a transformation corresponding to the "best" fitting-model was applied to perform a LME regression analysis. Otherwise, no transformation was made. Next, we used the LME regression models with random slopes and intercepts to analyze association between individual texture features and tumor anatomic volume. Analysis was performed for two fixed effect variables: Type (HM and NL) and Volume (VOI volume). The Volume was considered as a primary variable and the Type was considered as a fixed factor that could affect the Intercept and Slope. Therefore, the model could be summarized as follows:

$$\text{Normal Liver: Feature} = \text{Intercept} + \text{Slope} \times \text{Volume}$$

$$\text{Hepatic Metastases: Feature} = (\text{Intercept} + \Delta) + (\text{Slope} + \delta) \times \text{Volume}$$

where   is the intercept difference and δ is the slope difference of the LME regression. If the slope or the slope difference were statistically significant, then the effect of the size was considered to be important. The subject effect (e.g., sampling procedure) was considered as a random factor that accounts to the correlations between HM and NL measurements on the same subject. The contribution of each factor, as well as interaction effects were tested for significance. To assess the ability of features to discriminate between HM and NL, model performance and 95% confidence intervals (CI) were assessed by the area under the receiver operating characteristics (ROC) curve for each texture feature, results of the corresponding fitting model and the residuals. AUC above 0.7 was considered to ensure a fair classification accuracy, whereas AUC bellow 0.7 was indicative of a poor classification accuracy. The residuals were calculated as the difference between the measured texture features and the regression line.

Data analysis was performed using SPSS software version 25.0.0 (IBM Corporation, Somers, NY).

Results

We quantified the texture of LHM and NL simultaneously. Quantitative texture features for HM and NL are shown in Table 1. The skewness, kurtosis, and results of Shapiro-Wilk test confirmed normality assumption only for mean attenuation (SE = 0.15, RKU = 0.11, p = 0.75 for HM and SE = 0.03, RKU = 0.87, p = 0.53 for NL) and SD (SE = 0.45, RKU = 0.14, p = 0.21 for HM and SE = −0.07, RKU = −0.2, p = 0.97 for NL) for both HL and NL. The mean difference between NL and HM for the mean attenuation was 26 ± 4 HU (95% CI 18.6-33.7, p = 0.02) and for SD was 14 ± 1 HU (95% CI 12.2-15.3, p<0.001). The Mann-Whitney U test showed a significant intergroup difference for all other features (S1 Table).

Figure 2, Figure 3 provide a visual representation of the first and second-order (GLCM) texture features as a function of VOI's volume for both HM and NL. In addition, we applied the Spearman's rank correlation test for both HM and NL. For the first-order features (Table 1), the Spearman's rank correlation test was not statistically significant, with the exception of SD for normal liver ($p = 0.001$). In contrast, all GLCM texture features showed statistically significant correlation with VOI's volume, except only GLCM homogeneity ($p = 0.08$) for normal liver.

To examine the effect of size further, we applied a LME regression models. Due to nonlinear relationships between texture features and the VOI's volume, we examined relationships between texture features and VOI volume using five different fitting models. Table 2 shows the coefficient of determination, R-squared, and the results of Shapiro-Wilk's testing the residuals for normality. For the first-order texture features all fitting models demonstrated extremely low performance of R-squared. In contrast, R-squared for the GLCM features varied in range from 0.43 to 0.96 for HM, while for normal liver it was acceptable only for the GLCM energy (0.95) and the entropy (0.8). The Shapiro-Wilk test for normality of residuals was acceptable for all GLCM features except the GLCM heterogeneity for NL and, therefore, supporting the application of LME regression analysis. As a result, the power model was selected for the GLCM homogeneity, the inverse model was selected for the GLCM energy, the contrast and the dissimilarity, and the logarithmic model was selected for the GLCM correlation and the entropy. First order features were analyzed without any transformation.

The results of the LME regression analysis are summarized in Table 2. Each column shows the estimated value, the 95% CI (in parenthesis), and the statistical significance. The intercept and the slope represent the linear regression coefficients for the texture features from the NL, while the intercept difference and the slope difference represent a deviation of the HM regression coefficients from the ones derived for NL. For the NL, the intercept was not significantly different from zero only for the histogram skewness (p = 0.48), while the slope was not significant for all first-order features and the GLCM homogeneity ($p = 0.64$). For all other GLCM features the slope was statistically significantly different from zero. The intercept difference between HM and NL was not significant for the histogram kurtosis ($p = 0.08$) and the GLCM homogeneity ($p = 0.56$). The slope difference was not significant for all first-order features and it was significant for all GLCM features.

The texture features were compared between NL and HM using the area under the ROC curve. In addition, Table 3 shows performance of the fitting models was assessed by the area under the ROC curve for each fitting model and residuals. All first-order and second-order GLCM features demonstrated statistically significant difference for measurements and fitted model. AUC for GLCM features was varying in the range from 0.74 to 0.84, while for the first-order features the range was much wider, from 0.65 to 0.98.

Discussion

In this paper, we analyzed the dependence of the first-order histogram-based features and second-order 3D GLCM texture features on the VOI's volume. Initially, the GLCM features

were developed to analyze large-scale nonmedical images, thus assuming to be independent of ROI size (29). However, in case of finite size VOI that are common in medical imaging, we found statistically significant size dependence of all GLCM texture features on the VOI's volume for both HM and background liver. Moreover, some GLCM texture features demonstrated a difference in the size dependence between NL and HM.

Our results suggest that the GLCM texture feature size dependence emerges as a result of two factors: (1) the GLCM dependence on the number of voxels inside the VOI (finite size effect) and (2) the sensitivity of the GLCM to variations in the tissue texture that might be related to the tumor tissue development, such as necrosis, as well as development of texture heterogeneities in response to the therapy. We found that some features exhibited a similarity in the size dependence. For example, the energy and the entropy demonstrated a comparable behavior that can be explained by the way these features are calculated. In particular, energy is a sum of squared elements of the GLCM, while the entropy is a sum of the product of the GLCM element and its logarithm. These features demonstrate a similar size dependence because both of these functions are monotonic and the sum of them depends only on GLCM. On the other hand, features like the GLCM homogeneity, the contrast, the correlation and the dissimilarity, depend on both the GLCM and the voxel attenuation and demonstrated the difference in the size dependence between NL and HM. Therefore, one can conclude, that the combination of the GLCM and the voxel attenuation is more sensitive to the distribution of heterogeneities than the GLCM alone and, thus, could be more discriminatory to different types of tissue. Also, this finding suggests a route to design new radiomic features with higher tissue-type selectivity.

Interestingly, a strong correlation between tumor heterogeneity and anatomic tumor volume (24,26), as well as metabolically active tumor volume (24) were recently reported for different types of cancers. L. Dercle et al. revealed the logarithmic association between ROI area and Shannon's entropy for various type of metastasis, normal psoas muscle, and blood in the aorta (26). Hatt et al. (2015) demonstrated a significant interaction between two radiomic features (entropy and dissimilarity) and metabolically active tumor volume (24). However, the association with the cancer type was explained by differences in VOI's volume distributions, rather than the cancer-specific tissue heterogeneities. Also, changes in the value of texture features could provide an additional complementary information for response assessment in patients with liver metastases. For example, changes in the texture features extracted from the pretreatment and the post-treatment images could potentially identify early signs of response, progression, or cancer recurrence. However, appropriate methods for extracting clinically relevant information that is not affected by the feature extraction algorithms and parameters are still in early stage of development.

Technical aspect associated with the imaging techniques could also contribute to the association between texture features and tumor size. Volumetric texture features, in general, are calculated using 4 in-plane (axial) and 9 out-of-plane directions to spatially adjacent slices above and below the original one. Therefore, 3D texture features depend on two length scales defined by the image acquisition parameters – voxel size and interslice spacing distance. In case of CT or MR imaging texture analysis, the voxel size can be one-order of magnitude smaller than the interslice spacing distance. This implies that with

a gradual increase in tumor volume the contribution from out-of-plane voxels will increase, thus changing the balance from the description of 2D axial in-plane heterogeneities to a combination of both in-plane and out-of-plane (orthogonal to axial) heterogeneities.

We analyzed various models to quantify the size dependence. For some features, this analysis resulted in considerably high accuracy of the regression analysis. For example, fitting the GLCM energy and entropy with inverse and logarithmic functions resulted in substantially high coefficient of determination, R-squared >0.8. However, the primary objective of the measurements fitting was to transform measurements to satisfy linear (LME) regression analysis, rather than to develop a theoretically (functional) model. Therefore, future works should include a theoretical analysis of VOI's volume effect on GLCM and more comprehensive analysis of the size dependence in the small and large-volume limits, where different trends are expected. Also, the texture features size-dependence association with the cancer type, as well as the effect of therapy, is of a great interest for further studies.

There were several limitations to our study that warrant mention. First, this was a retrospective study with a limited sample size. Texture analysis was limited to only the first-order histogram based and second-order (GLCM) texture features in order to conduct a comprehensive analysis. Another limitation to this study is the fact that almost all liver lesions were treated and the treatment period varied. The variability in the treatment protocols adds another degree of freedom into our model since various locoregional therapies are known to have different effects on the NL and hepatic lesions. However, the size dependence between NL and HM groups was significantly different for the second-order GLCM texture features. Another limitation to this study is the fact that the analysis was performed only for liver metastasis of one type of cancer.

Conclusion

Higher-order radiomic features of breast cancer hepatic HMize dependence. This finding demonstrates the complex behavior of imaging features and the need to include feature specific properties into radiomic models. Caution should be exercised when directly comparing radiomic features of different size tumors.

Supplementary Material

Refer to Web version on PubMed Central for supplementary material.

Acknowledgments

References

1. Tan DS, Thomas GV, Garrett MD, et al. Biomarker-driven early clinical trials in oncology: a paradigm shift in drug development. Cancer J 2009; 15:406–420. [PubMed: 19826361]

2. Eisenhauer EA, Therasse P, Bogaerts J, et al. New response evaluation criteria in solid tumours: revised RECIST guideline (version 1.1). Eur J Cancer 2009; 45:228–247. doi:10.1016/j.ejca.2008.10.026. [PubMed: 19097774]

3. Therasse P, Arbuck SG, Eisenhauer EA, et al. New guidelines to evaluate the response to treatment in solid tumors. J Natl Cancer Inst 2000; 92:205–216. [PubMed: 10655437]

4. Choi H, Charnsangavej C, Faria SC, et al. Correlation of computed tomography and positron emission tomography in patients with metastatic gastrointestinal stromal tumor treated at a single institution with imatinib mesylate: proposal of new computed tomography response criteria. J Clin Oncol 2007; 25:1753–1759. doi:10.1200/JCO.2006.07.3049. [PubMed: 17470865]

5. Ronot M, Bouattour M, Wassermann J, et al. Alternative response criteria (Choi, European Association for the Study of the Liver, and Modified Response Evaluation Criteria in Solid Tumors [RECIST]) versus RECIST 1.1 in patients with advanced hepatocellular carcinoma treated with sorafenib. Oncologist 2014; 19:394–402. doi:10.1634/theoncologist.2013-0114. [PubMed: 24652387]

6. Vera R, Gomez Dorronsoro M, Lopez-Ben S, et al. Retrospective analysis of pathological response in colorectal cancer liver metastases following treatment with bevacizumab. Clin Trans Oncol 2014; 16:739–745. doi:10.1007/s12094-013-1142-x.

7. Wolchok JD, Hoos A, Day S, et al. Guidelines for the evaluation of immune therapy activity in solid tumors: immune-related response criteria. Clin Cancer Res 2009; 15(23):7412. [PubMed: 19934295]

8. Seyal AR, Parekh K, Velichko YS, et al. Tumor growth kinetics versus RECIST to assess response to locoregional therapy in breast cancer liver metastases. Acad Radiol 2014; 21(8):950–957. doi:10.1016/j.acra.2014.02.015 [PubMed: 24833565]

9. Villaruz LC, Socinski MA. The Clinical Viewpoint: Definitions, Limitations of RECIST, Practical Considerations of Measurement. Clin Cancer Res 2013; 19:2629. [PubMed: 23669423]

10. Gillies RJ, Kinahan PE, Hricak H. Radiomics: images are more than pictures, they are data. Radiology 2015; 78:563–577. doi:10.1148/radiol.2015151169.

11. Kumar V, Gu Y, Basu S, et al. Radiomics: the process and the challenges. Magn Reson Imaging 2012; 30:1234–1248. doi:10.1016/j.mri.2012.06.010. [PubMed: 22898692]

12. Lambin P, Rios-Velazquez E, Leijenaar R, et al. Radiomics: extracting more information from medical images using advanced feature analysis. Eur J Cancer 2012; 48:441–446. doi:10.1016/j.ejca.2011.11.036. [PubMed: 22257792]

13. Marusyk A, Almendro V, Polyak K. Intra-tumour heterogeneity: a looking glass for cancer? Nat Rev Cancer 2012; 12:323–334. [PubMed: 22513401]

14. Burrell RA, McGranahan N, Bartek J, et al. The causes and consequences of genetic heterogeneity in cancer evolution. Nature 2013; 501(7467):338–345. doi:10.1038/nature12625. [PubMed: 24048066]

15. Alic L, Niessen WJ, Veenland JF. Quantification of heterogeneity as a biomarker in tumor imaging: a systematic review. PLOS One 2014; 9:e110300 doi:10.1371/journal.pone.0110300. [PubMed: 25330171]

16. Young JR, Margolis D, Sauk S, et al. Clear cell renal cell carcinoma: discrimination from other renal cell carcinoma subtypes and oncocytoma at multi-phasic multidetector CT. Radiology 2013; 267:444–453. doi:10.1148/radiol.13112617. [PubMed: 23382290]

17. Fan M, Wu G, Cheng H, et al. Radiomic analysis of DCE-MRI for prediction of response to neoadjuvant chemotherapy in breast cancer patients. Eur J Radiol 2017; 94:140–147 10.1016/j.ejrad.2017.06.019. [PubMed: 28712700]

18. Sun R, Limkin EJ, Vakalopoulou M, et al. A radiomics approach to assess tumour-infiltrating CD8 cells and response to anti-PD-1 or anti-PD-L1 immunotherapy: an imaging biomarker, retrospective multicohort study. Lancet Oncol 2018;19:1180–1191. [PubMed: 30120041]

19. Sebastian B, Daniel P, Philipp K, et al. Prediction of malignancy by a radiomic signature from contrast agent-free diffusion MRI in suspicious breast lesions found on screening mammography. J Magn Reson Imaging 2017; 46:604–616. doi:10.1002/jmri.25606. [PubMed: 28152264]

20. Prasanna P, Tiwari P, Madabhushi A. Co-occurrence of Local Anisotropic Gradient Orientations (CoLlAGe): a new radiomics descriptor. Sci Rep 2016; 6:37241. doi:10.1038/srep37241. [PubMed: 27872484]

21. Guo W, Li H, Zhu Y, et al. Group TBPR Prediction of clinical phenotypes in invasive breast carcinomas from the integration of radiomics and genomics data. SPIE, 2015:12.

22. Li R, Xing L, Napel S, Rubin DL. Radiomics and radiogenomics: technical basis and clinical applications. Chapman and Hall/CRC, 2019.

23. Miles K. Radiomics for personalised medicine: the long road ahead. Nature Publishing Group, 2020.

24. Hatt M, Majdoub M, Vallieres M, et al. 18F-FDG PET uptake characterization through texture analysis: investigating the complementary nature of heterogeneity and functional tumor volume in a multicancer site patient cohort. J Nuc Med 2015; 56:38–44. doi:10.2967/jnumed.114.144055.

25. Zhao B, Tan Y, Tsai WY, et al. Reproducibility of radiomics for deciphering tumor phenotype with imaging. Sci Rep 2016; 6:23428. doi:10.1038/srep23428. [PubMed: 27009765]

26. Dercle L, Ammari S, Bateson M, et al. Limits of radiomic-based entropy as a surrogate of tumor heterogeneity: ROI-area, acquisition protocol and tissue site exert substantial influence. Sci Rep 2017; 7:7952. doi:10.1038/s41598-017-08310-5. –7952. [PubMed: 28801575]

27. Shafiq-ul-Hassan M, Latifi K, Zhang G, et al. Voxel size and gray level normalization of CT radiomic features in lung cancer. Sci Rep 2018; 8:10545. doi:10.1038/s41598-018-28895-9. [PubMed: 30002441]

28. Nioche C, Orlhac F, Boughdad S. A freeware for tumor heterogeneity characterization in PET, SPECT, CT, MRI and US to accelerate advances in radiomics. J Nuc Med 2017; 58(supplement 1):1316.

29. Haralick RM, Shanmugam K, Dinstein I. Textural features for image classification. IEEE Trans Syst Man Cybernet SMC 1973; 3:610–621. doi:10.1109/TSMC.1973.4309314.

30. Parekh V, Jacobs MA. Radiomics: a new application from established techniques. Expert Rev Precis Med Drug Dev 2016; 1:207–226. doi:10.1080/23808993.2016.1164013. [PubMed: 28042608]
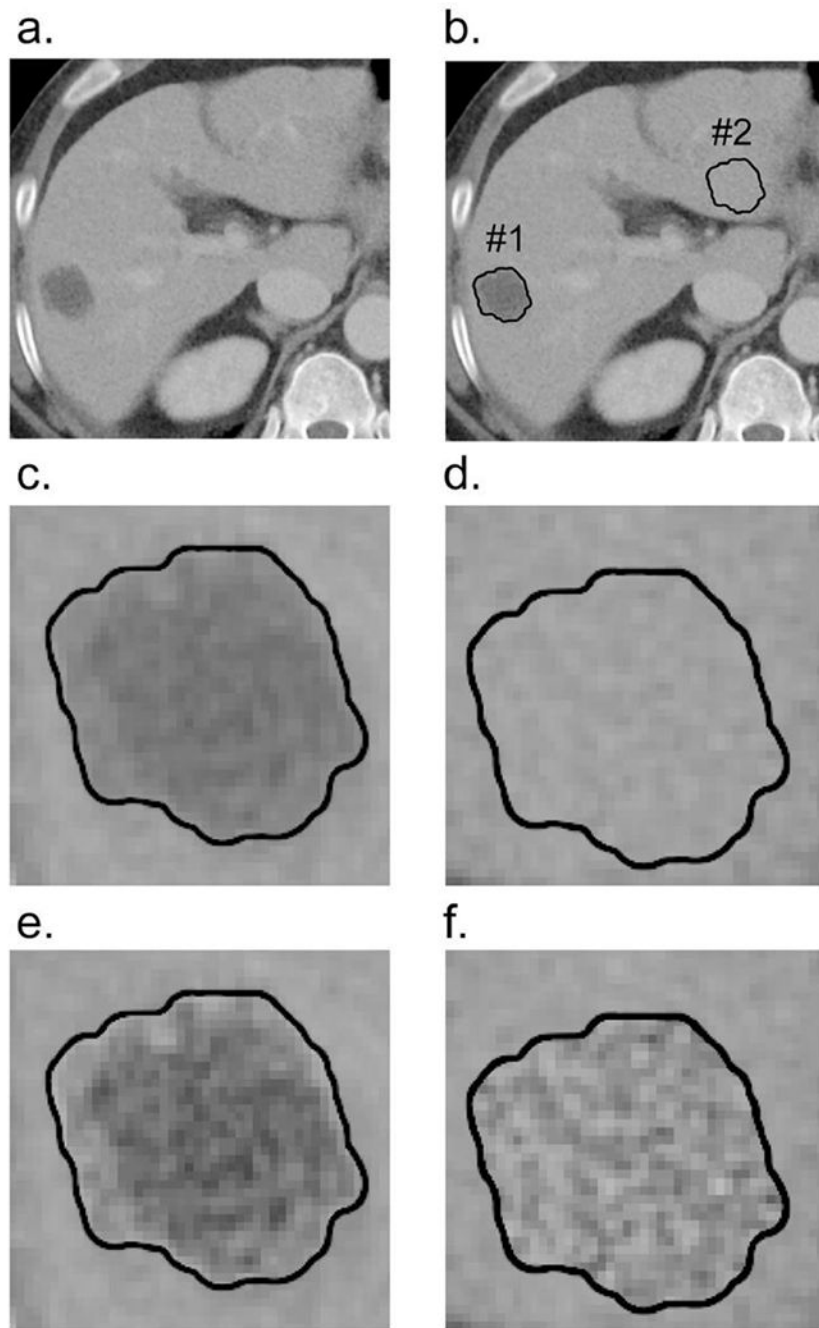
Figure 1.
(a) Representative example of axial contrast-enhanced CT scan in a 69-year-old patient with the breast cancer liver metastasis. (b) Hepatic metastasis segmentation (ROI #1) and normal liver segmentation (ROI #2) are marked by a contour lines. Close-up view of (c) the hepatic metastasis and (d) the normal liver segmentations. Image intensity adjusted close-up view of (e) the hepatic metastasis and (f) the normal liver segmentation.
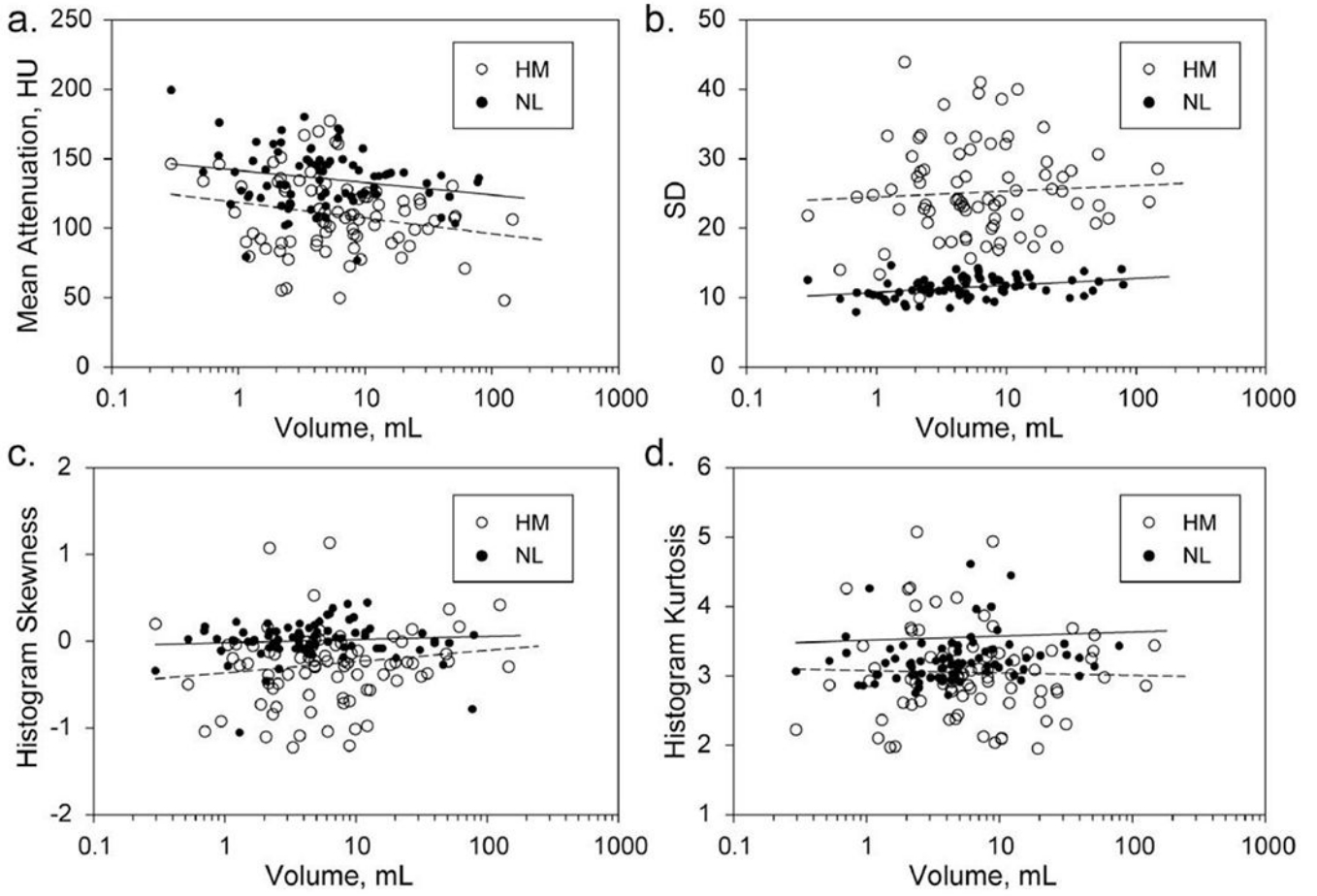
Figure 2.
First-order histogram based features as a function of VOI's volume for both hepatic metastasis and normal liver: (a) mean attenuation, (b) standard deviation, (c) histogram skewness, and (d) histogram kurtosis.
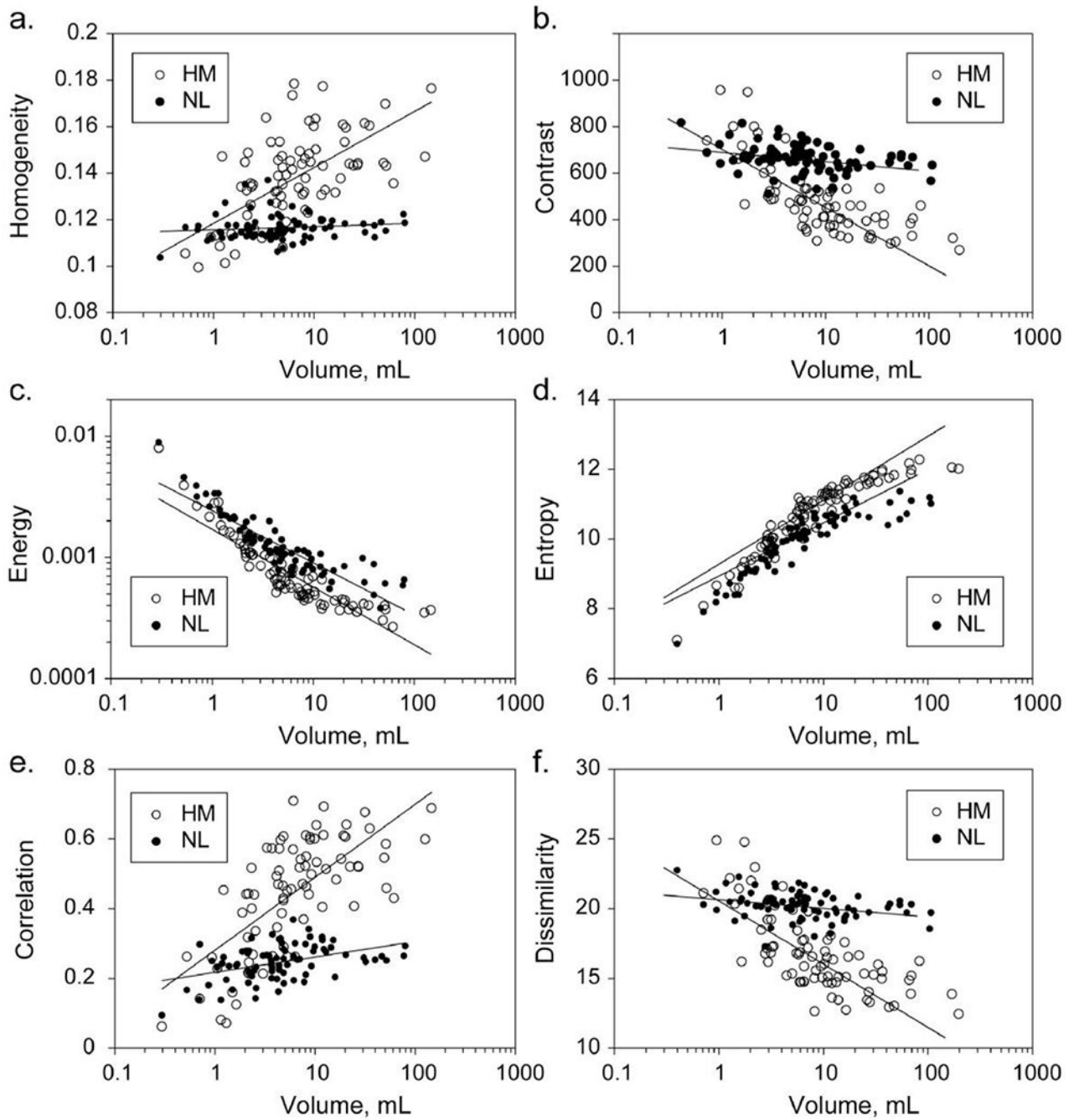
Figure 3.
Second order 3D GLCM features as a function of VOI's volume for both hepatic metastasis and normal liver: (a) GLCM homogeneity, (b) GLCM contrast, (c) GLCM energy, (d) GLCM entropy, (e) GLCM correlation, and (f) GLCM dissimilarity.

Table 1.

Qualitative analysis of 3D radiomic features of hepatic metastatic and normal liver of 54 patients with breast cancer

	Type	Mean (SD)	Median (Range)	Skewness	Kurtosis	Shapiro-Wilk, p	Spearman Rank, p
Mean value	HM	109.6 ± 27.1	108 (48 to 177)	0.15	0.11	0.754	0.111
	NL	135.8 ± 21.2	137 (77 to 199)	0.03	0.87	0.527	0.179
SD	HM	25.1 ± 6.9	23.4 (9.9 to 43.9)	0.45	0.14	0.214	0.718
	NL	11.4 ± 1.4	11.4 (7.9 to 14.6)	−0.07	−0.2	0.971	0.001
Histogram skewness	HM	−0.26 ± 0.44	−0.22 (−1.2 to 1.2)	1.54	0.01	0.006	0.283
	NL	0.006 ± 0.33	0.04 (−1.9 to 0.5)	−3.7	18.6	<0.001	0.524
Histogram kurtosis	HM	3.1 ± 0.6	2.9 (1.9 to 5.1)	0.7	0.9	0.013	0.825
	NL	3.2 ± 1.6	3.2 (2.7 to 14.4)	5.3	30.5	<0.001	0.052
GLCM homogeneity	HM	0.14 ± 0.02	0.14 (0.08 to 0.18)	−0.3	0.4	0.343	<0.001
	NL	0.116 ± 0.005	0.12 (0.1 to 0.14)	0.8	2.5	0.004	0.084
GLCM energy	HM	0.001 ± 0.001	0.0006 (0.0 to 0.01)	4.7	28.1	<0.001	<0.001
	NL	0.0015 ± 0.001	0.0011 (0.0 to 0.01)	3.8	20.2	<0.001	<0.001
GLCM contrast	HM	504 ± 176	469 (270 to 1330)	1.84	5.43	<0.001	<0.001
	NL	662 ± 58	665 (510 to 817)	0.11	0.75	0.215	0.002
GLCM correlation	HM	0.44 ± 0.16	0.47 (0.06 to 0.71)	−6.46	−0.33	0.002	<0.001
	NL	0.25 ± 0.05	0.25 (0.09 to 0.37)	−0.42	0.27	0.570	<0.001
GLCM entropy	HM	10.7 ± 1.0	11 (7.1 to 12.3)	−1.0	0.99	<0.001	<0.001
	NL	10.0 ± 0.8	10.1 (6.9 to 11.4)	−0.95	0.95	0.001	<0.001
GLCM dissimilarity	HM	17.0 ± 3.2	16.3 (12.5 to 31.0)	1.55	3.8	<0.001	<0.001
	NL	20.2 ± 0.9	20.3 (17.3 to 22.8)	−0.22	0.85	0.579	0.003

Table 2.

Summary Table of Linear Mixed-Effects Regression Analysis of 3D Radiomic Features of Hepatic Metastatic and Normal Liver of Patients with Breast Cancer

	Model	Normal Liver				Hepatic Metastasis Deviation from the Normal Liver			
		Intercept (95% CI)	p	Slope (95% CI)	p	(95% CI)	p	δ (95% CI)	p
Mean attenuation	Linear	138.5 (131 to 145)	<0.001	−0.19 (−0.5 to 0.1)	0.20	−25.4 (−31 to −19)	<0.001	−9.4E-3 (−0.3 to 0.3)	0.955
SD	Linear	11.1 (9.7 to 12.4)	<0.001	0.32 (−0.04 to 0.1)	0.38	14.0 (12.4 to 15.6)	<0.001	−0.27 (−0.1 to 0.05)	0.523
Histogram skewness	Linear	0.04 (−0.07 to 0.14)	0.48	3E-3 (−8E-3 to 2.5E-3)	0.28	−0.34 (−0.47 to −0.21)	<0.001	6.3E-3 (−2.3E-4 to 0.13)	0.059
Histogram kurtosis	Linear	3.4 (3.1 to 3.7)	<0.001	0.014 (−4.6E-3 to 0.03)	0.14	−0.39 (−0.93 to 0.05)	0.08	−0.01 (−0.03 to 0.01)	0.250
GLCM homogeneity	Power	−0.94 (−0.95 to −0.92)	<0.001	3.9E-3 (−0.01 to 0.02)	0.64	5.5E-3 (−0.01 to 0.02)	0.56	0.08 (0.06 to 0.1)	<0.001
GLCM energy	Inverse	6.2E-4 (5.5E-4 to 6.8E-4)	<0.001	2.3E-3 (2.2E-3 to 2.4E-3)	<0.001	−3.6E-4 (−4E-4 to −3E-4)	<0.001	−1.7E-4 (−4.7E-4 to −3E-4)	0.007
GLCM contrast	Inverse	644 (622 to 668)	<0.001	45 (9 to 82)	<0.001	−235 (−264 to −205)	<0.001	255 (205 to 305)	<0.001
GLCM correlation	Log	0.22 (0.19 to 0.25)	<0.001	0.04 (0.001 to 0.08)	<0.001	0.06 (0.02 to 0.11)	0.007	0.17 (0.11 to 0.21)	<0.001
GLCM entropy	Log	8.96 (8.81 to 9.1)	<0.001	1.49 (1.32 to 1.66)	<0.001	0.35 (0.16 to 0.54)	<0.001	0.3 (0.07 to 0.52)	0.009
GLCM dissimilarity	Inverse	20 (19.5 to 20.4)	<0.001	0.7 (0.006 to 1.4)	0.04	−4.6 (−5.2 to −4.1)	<0.001	4.6 (3.6 to 5.4)	<0.001

Table 3.

Summary of AUC (Area under the curve) for measurements, fitting model and residuals for 3D radiomic features of hepatic metastatic and normal liver of patients with breast cancer

	Measurements		Fitting Model			Residuals	
	AUC (95% CI Range)	p	Model	AUC (95% CI Range)	p	AUC (95% CI Range)	p
Mean attenuation	0.78 (0.71 to 0.86)	<0.001	**Linear**	1.0 (1.0 to 1.0)	<0.001	0.51 (0.42 to 0.6)	0.89
SD	0.98 (0.96 to 1.0)	<0.001	**Linear**	1.0 (1.0 to 1.0)	<0.001	0.56 (0.46 to 0.66)	0.22
Histogram skewness	0.77 (0.69 to 0.85)	<0.001	**Linear**	0.97 (0.94 to 1.0)	<0.001	0.51 (0.42 to 0.6)	0.82
Histogram kurtosis	0.65 (0.56 to 0.74)	0.002	**Linear**	1.0 (1.0 to 1.0)	<0.001	0.64 (0.55 to 0.73)	0.02
GLCM homogeneity	0.83 (0.76 to 0.91)	<0.001	**Power**	0.96 (0.91 to 1.0)	<0.001	0.51 (0.4 to 0.59)	0.91
GLCM energy	0.78 (0.7 to 0.85)	<0.001	**Inverse**	0.78 (0.7 to 0.85)	<0.001	0.53 (0.44 to 0.62)	0.57
GLCM Contrast	0.83 (0.76 to 0.90)	<0.001	**Inverse**	0.92 (0.86 to 0.98)	<0.001	0.54 (0.44 to 0.63)	0.43
GLCM correlation	0.85 (0.78 to 0.92)	<0.001	**Log**	0.97 (0.93 to 1.0)	<0.001	0.52 (0.42 to 0.61)	0.72
GLCM entropy	0.74 (0.66 to 0.82)	<0.001	**Log**	0.74 (0.67 to 0.82)	<0.001	0.5 (0.41 to 059)	0.93
GLCM dissimilarity	0.84 (0.77 to 0.91)	<0.001	**Inverse**	0.94 (0.89 to 0.99)	<0.001	0.54 (0.44 to 0.63)	0.41